Three-dimensional mineral dendrites reveal a non-classical crystallization pathway

Zhaoliang Hou[1], Dawid Woś[2], Cornelius Tschegg[3], Anna Rogowitz[4,1], A. Hugh N. Rice[1], Lutz Nasdala[5], Florian Fusseis[6], Piotr Szymczak[2*], Bernhard Grasemann[1*]

[1]*Department of Geology, University of Vienna, Vienna 1090, Austria*

[2]*Institute of Theoretical Physics, University of Warsaw, Warsaw 02-093, Poland*

[3]*Glock Health, Science and Research GmbH, Deutsch-Wagram 2232, Austria*

[4]*Institute for Earth Sciences, University of Graz, Graz 8010, Austria*

[5]*Institute of Mineralogy and Crystallography, University of Vienna, Vienna 1090, Austria*

[6]*School of Geosciences, University of Edinburgh, Edinburgh EH9 3FE, UK*

ABSTRACT

Manganese (Mn) dendrites are a common type of mineral dendrite that typically forms two-dimensional structures on rock surfaces. Three-dimensional (3D) Mn dendrites in rocks have rarely been reported, hence their growth implications have largely escaped attention. Here, we combine high-resolution X-ray and electron-based data with numerical modelling to give the first detailed description of natural 3D Mn dendrites (in clinoptilolite tuffs) and elucidate their growth dynamics. Our data show that 3D dendrite growth occurred by accretion of Mn oxide nanoparticles formed when Mn-bearing fluids mixed with oxygenated pore-water. The geometry of the resulting structures is sensitive to ion concentrations, the volume of infiltrating fluid, and the number of fluid pulses; thus 3D dendrites record the hydro-geochemical rock history.

INTRODUCTION

In contrast to metallic/crystalline dendrites formed by solidification of supercooled melts (Trivedi and Kurtz, 1994), mineral dendrites are a fingerprint of unstable aqueous growth processes, driven by an interplay between fluid motion and chemical concentration gradients (Chopard et al., 1991; Ruiz et al., 1994, Meakin and Jamtveit, 2010). Mn mineral dendrites form by oxidative precipitation of Mn and typically grow as planar two-dimensional structures on rock surfaces (Chopard et al., 1991; Ruiz et al., 1994). Although 3D Mn dendrites have been reported (Van Straaten 1978), their growth processes remain enigmatic. 3D gold/electrum dendrites from epithermal conditions are better studied (Saunders, 2020, Monecke, 2023).

We studied natural 3D Mn dendrites with combined micro-scale analyses and numerical modelling (Supplemental material 1). The data show that our dendrites encode the hydro-geochemical history of the rock, including the number and relative volumes of infiltrating Mn-rich fluid pulses. We also show that dendrite growth proceeded through the formation, diffusion and attachment of Mn oxide nanoparticles, a non-classical crystallization pathway increasingly recognized as an important crystal growth mechanism (De Yoreo et al., 2015; Hochella et al., 2019).

SAMPLE BACKGROUND

The Mn dendrites documented here occur in clinoptilolite tuffs at Nižný Hrabovec (Slovak Republic; Fig. 1A; Supplemental material Fig. S2A). The chemically and mineralogically homogeneous 16.3-15 Ma old tuff formed from pure rhyolitic volcanic ash that was zeolitized at 44-84°C (Tschegg et al., 2019). The tuff has abundant inter- and intragranular pores, allowing fluid-borne metals to diffuse into clinoptilolite grains and be loosely sorbed in the crystal lattice (Tschegg et al., 2020).

Dendrites are formed by different mineral associations, their composition being neither singular nor universal. Our dendrites comprising amorphous Mn-oxides (Supplemental material Fig. S3), grew adjacent and perpendicular to Mn coated fractures in the tuffs. To simplify descriptions, we take as a local reference frame the fractures to be horizontal and "below" and dendrites to grow "upwards".

MORPHOLOGY OF 3D DENDRITES

X-ray microtomography reveals a 3D dendrite "forest" in the clinoptilolite tuff (Fig. 1B; Movie S1). Overall, the < 15 mm high forest has a volume-fraction of ~23% (107 mm^3 in 467 mm^3 rock), with dendrite abundance decreasing with a power-law scaling with forest height (Supplemental material Fig. S2C). All dendrites have a core surrounded by a ~17 µm thick outer rim (Fig. 1C). The forest base, which lies adjacent to the fracture surface, comprises a continuous layer of dendrite core material, with only small, irregular holes remaining (Fig. 1D), connecting the fracture void to the clinoptilolite tuff. The dendrites have a straight, sub-circular primary trunk with a botryoidal surface morphology and a scallop-like top (Fig. 1B). Short conical to cylindrical branches make the dendrite shape increasingly bulky upwards, reflected in a slight increase in the forest's 3D fractal dimension, from ~2.70 to 2.80 (Supplemental material Fig. S2D).

Digital microscope data on polished sections oriented normal to fractures characterize the forest geometry (Fig. 1E). Four non-overlapping conical branch groups formed during dendrite growth (Bi-Biv), shown by fluctuations in the combined dendrite width (Fig. 1F) and the average individual dendrite width (Fig. 1G): Bi lies at 0 - 2.3 mm from the forest base, Bii at 2.3 - 4.7 mm, Biii at 4.7 - 11.4 mm and Biv at >11.4 mm. Total dendrite width decreases from ~16.1 to

0.9 mm (Fig. 1F) and average dendrite width increases from ~154 µm to 383 µm from Bi to Biv (Fig. 1G). Dendrite volume-fractions decrease from ~40 to 0% (Supplemental material Fig. S4).

Individual dendrites all have a trunk-domain at the base and a branching-domain further up (Fig. 2A). Branching-domains widen towards dendrite-tops, especially Biii and Biv, within which the dendrites develop a concentric architecture comprising alternating layers of core and rim material (Fig. 2A, B). All dendrites in a sample have the same number of internal layers at a given distance from the fracture surface (Fig. 2B).

CHEMISTRY AND MICROSTRUCTURES

Scanning electron microscope (SEM) observations of thin-sections show that dendrite growth reduced the original porosity from ~17% in the matrix to ~1 to 4% in the internal rims, and 0% in the cores (Fig. 2C-E, C'-E'). The outer rims adjacent to the matrix, have a steep porosity gradient, from 17 to 4% (Fig. 2A'-C'). Electron probe micro-analyzer (EPMA) line-scans across dendrites and into the matrix indicate that Mn concentrations are linked to dendrite core-rim architecture (Fig. 2A, B). Increasing Mn concentrations from matrix to core are accompanied by an exponential drop in porosity (Fig. 2F), and a linear decrease in silicon concentration (Fig. 2G). No Mn is present in the matrix (Fig. 2G). Rim Mn concentrations vary between 1.3 - 7.7 wt% and cores between 8.0 - 19.3 wt%. In contrast, the silicon drops from the matrix (6.7 wt% variation) to the cores (~3.5 wt % variation at a given Mn concentration; Fig. 2G). Silicon was not mobile but the addition of Mn oxides reduced its proportion.

High-resolution SEM images show sub-angular to rounded, several nm to 1 µm sized (average 380 nm) Mn oxide nanoparticles in dendrites (Fig. 3A, B) but not the matrix (Fig. 3C). These particles form larger aggregates, rather than being individually distributed and randomly attached to the rock (Fig. 3B). Although the nanoparticle aggregates look the same in cores and

rims, they occur in different pore contexts. In the cores, BSE images show that Mn oxide completely fills both inter- and intragranular pores and is also sorbed into the clinoptilolite crystal lattice (confirmed by EPMA). Only the centers of large clinoptilolite grains (>13 μm size) are free of Mn oxides, although infiltration into marginal intragranular pores occurred (Fig. 3D). In the rims, intergranular pores are filled by Mn oxide, but intragranular pores are unaffected (Fig. 3E). No Mn oxide is observed in the matrix (Fig. 3F).

DISCUSSION AND CONCLUDING REMARKS

Dendrite growth processes

Since the tuff was initially chemically and mineralogically homogeneous, and without heavy-metals, a pulse of Mn-rich fluid must have infiltrated the rock through pre-existing fractures. We hypothesize that the fluid pushed an oxygenated matrix pore fluid away from the fracture and mixed with it, generating an oversaturated Mn oxide solution (Fig. 4A, b0). Laboratory studies on Mn oxide (Li et al., 2014; Huang et al., 2015) confirm that such conditions promote the initial growth of Mn oxide nanoparticles. This is consistent with our observation of Mn oxide particles on dendrite surface (Fig. 3A, B). We thus propose that Mn oxide particles formed in the pore fluid, diffused through the rock matrix and became attached to the Mn oxide-coated fracture (Fig. 4A, b1), initiating dendrite growth. Such a non-standard crystallization pathway, via particle attachment, is increasingly recognized as an important and widespread type of crystal growth (Ivanov et al., 2014; De Yoreo et al., 2015; Hochella et al., 2019).

Since the fractal dimension of the dendrites increases with increasing length-scales, the dendrite forest is not completely scale-free. This is likely due to the relatively high Mn particle concentration prevailing during dendrite growth, implying the existence of finite concentration effects. This leads to the formation of a diffusive boundary layer and hence introduces an

additional length scale into the system (Voss, 1984; Meakin et al., 1984, Fowler et al. 1989). Variations in dendrite abundance and width (Bi to Biv) demonstrate that dendrites competed for nanoparticles. Such competitive dynamics lead to a power-law distribution of dendrite lengths $N(L) \sim L^{-\alpha}$, where N(L) denotes the number of dendrites longer than L (Krug, 1997). In our case, $\alpha \approx 1.25$ (Supplemental material Fig. S2C), in line with the scaling reported for similar fingered growth systems, such as dissolution channels (Szymczak and Ladd, 2006).

With ongoing dendrite growth, the Mn oxide nanoparticle concentration in the pore fluid decreased continuously (Fig. 4A, b2). At a certain concentration, the chemical potential gradient driving nanoparticle diffusion was insufficient to overcome the energy barrier for diffusion into intragranular pore space; thus clinoptilolite grains remained Mn oxide-free, and precipitation proceeded in intergranular pores only, sealing off the intragranular porosity, forming rim material (Fig. 4A, b3).

A unique feature of our dendrites is their banding, with alternating layers of core and rim material. Dendrites in a thin-section have the same number of core-rim layers at any given distance from the fracture, implying that the banding was due to overall changes in nanoparticle concentration in the pore fluid, rather than to local precipitation dynamics. The occurrence of rims only in the upper part of longer dendrites strongly suggests that growth proceeded by accretion of particles diffusing from above, in discrete pulses.

Each pulse of Mn-rich fluids pushed the interface with the oxygenated matrix pore fluid beyond the dendrites, creating a new batch of nanoparticles. By diffusion, these particles reached existing dendrites first, especially longer ones, attaching preferentially to their tips, overgrowing the existing rims and forming a new core layer (Fig. 4A, b4) and then, after nanoparticle depletion, a rim. When no further fluid pulses occurred, dendrite growth ceased.

The core-rim succession cannot be explained by the viscous fingering model for dendrite growth (Ruiz, 1994), which proposes that dendrites are fingers of infiltrating Mn-rich fluids that solidify by reacting with oxygen in the matrix. However, if this was the case, further pulses of fluid would not proceed along pre-existing dendrites, which have a small porosity, but rather in the porous material between existing dendrites, forming new dendrites. The banding structure is thus further evidence of particle attachment processes, triggered by fluid pulses.

Our model is thus more in line with the diffusion-limited aggregation model of Mn dendrite formation (Chopard et al., 1991), which suggests that they form by aggregation of diffusing particles, although the details of this process and the nature of the particles remains unspecified. Our model also shares features with growth models for gold/electrum dendrites (Schoenly & Saunders, 1993; Saunders, 2020), in which dendrites formed by accretion of colloidal particles created deep in hydrothermal systems and carried up to epithermal settings. An alternative mechanism for the growth of gold dendrites, based on ion addition, was proposed by Monecke et al. (2023).

Note that amorphous aggregation dendrites (like those studied here) are morphologically significantly different from crystalline dendrites growing in supercooled melts seen in metallurgy (Trivedi and Kurtz, 1994; Haxhimali et al., 2006). The latter are usually needle-like, with a strong dependence on crystal anisotropy and thermal effects. Petrologically, such dendritic crystals often form due to crystallization in rapidly cooled magmas (cf Welsch et al., 2013, Barbey et al., 2019).

Numerical modeling of dendrite growth

We numerically modelled dendrite formation using the lattice-Boltzmann method (Sukop & Thorne, 2006), tracking the diffusing populations of Mn ions and oxygen molecules as well as

the reaction between them that led to Mn oxide nanoparticles forming. The nanoparticle population was then tracked, as well as their aggregation on dendrite surfaces (Supplemental material 1.3). As shown in the morphological diagram (Fig. 4B, Supplemental material 1, Fig. S1A), the model gives a variety of structures, depending primarily on the concentrations of the reacting species as well as the magnitude of the surface energy. The morphologies range from highly branched, fractal aggregates with thin trunks, to bulkier structures, broadening upwards; this is consistent with our natural dendrite forest.

Based on parameters defined by the 2D models, a 3D model was run. The corresponding phase diagram is shown in Supplemental material 1, Fig. S1B. Comparison of the modelled dendrites with the natural structures suggests that Mn and oxygen concentrations should be the same order during dendrite formation, whereas the surface energy effects were in the intermediate range (κ~4.5).

The numerical dendrite morphologies are very similar to the natural examples (Fig. 4A, a1-a4; Movie S2). First, the decreasing total dendrite abundance and increasing dendrite width with greater distances from the fracture surface are reproduced by the model, as a result of growth competition between the individual dendrites. Second, the fractal dimension of 2.74 for the model is compatible with 2.7-2.8 in the natural system. Third, the dendrite volume-fraction as a function of the distance from the fracture in the numerical model is also similar to the natural forest (Supplemental material Fig. S4): there is a pronounced maximum at small distances, corresponding to the forest base and Bi, with volume-fractions up to 44%, followed by a plateau corresponding to Bii-iii, with volume-fractions of ~25%; for longer distances from the fracture plane the dendrite volume fraction sharply decreases.

Implications

Particle attachment processes are increasingly recognized as a non-classical but widespread and significant crystallization pathway (Ivanov et al., 2014; De Yoreo et al., 2015). Our work demonstrates that the growth of the 3D dendrite forest proceeded via particle attachment and, given the relative simplicity of the system, constitutes a perfect testing ground to investigate the interplay of diffusion and surface energy effects in the growth dynamics.

Our dendrites are a prime example of chemically-driven self-organization, with the system, initially driven out of equilibrium by external fluid pulses, returning to equilibrium by forming Mn oxide nanoparticles and then aggregating them into dendrites. The efficiency of this process is remarkable, since no Mn remains in the rock matrix. This suggests that particle formation and subsequent attachment to the dendrites could be an effective method for environmental remediation, as conjectured by De Yoreo et al. (2015). In this way, the spontaneous formation of 3D mineral dendrites can be seen as a "self-purification" of the porous medium, holding out the prospect for their use in environmental and groundwater remediation (e.g., Yeritsyan et al., 2013; Cataldo et al., 2021).

The particle attachment mechanism responsible for the growth of our dendrites has similarities with colloidal deposition models for the formation of gold/electrum dendrites (Schoenly and Saunders, 1993; Saunders and Burke, 2017; Saunders 2022). This might lead to a better understanding of the formation mechanism of ultrahigh-grade gold ("bonanza") veins (McLeish 2021).

Finally, since mineral dendrite growth is sensitive to the volume of infiltrating fluid and Mn ion concentrations, the dendrite structure encodes the hydrogeochemical history of the rock in itself.

ACKNOWLEDGMENTS

Funded by the Department of Geology, University of Vienna and Glock Health, Sciences and Research GmbH (Project ID: FA536901). Piotr Szymczak was funded by National Science Centre (NCN) under the CEUS-UNISONO Grant No. 2020/02/Y/ST3/00121. E. Matiasek is thanked for XRD work.

SUPPLEMENTAL MATERIALS

Supplemental material 1. Methods

Supplemental material Fig. S2. Sample description

Supplemental material Fig. S3. Dendrite geochemistry data

Supplemental material Fig. S4. Numerical Vs. Natural dendrites

Other supplemental materials including Movie S1, Movie S2.

REFERENCES

Barbey, P., Faure, F., Paquette, J.L., Pistre, K., Delangle, C. and Gremilliet, J.P., 2019, Skeletal quartz and dendritic biotite: Witnesses of primary disequilibrium growth textures in an alkali-feldspar granite: Lithos, v. 348, p.105202, https://doi.org/10.1016/j.lithos.2019.105202.

Cataldo, E., Salvi, L., Paoli, F., Fucile, M., Masciandaro, G., Manzi, D., Masini, C.M. and Mattii, G.B., 2021, Application of zeolites in agriculture and other potential uses: A review. Agronomy, v. 11, p. 1547, https://doi.org/10.3390/agronomy11081547.

Chopard, B., Herrmann, H.J. and Vicsek, T., 1991, Structure and growth mechanism of mineral dendrites: Nature, v. 353, p. 409-412, DOI:10.1038/353409a0.

De Yoreo, J.J et al., 2015, Crystallization by particle attachment in synthetic, biogenic, and geologic environments: Science, v. 349, p. aaa6760, DOI: 10.1126/science.aaa6760.

226 Fowler, A.D., Stanley, H.E. and Daccord, G., 1989, Disequilibrium silicate mineral textures:
227 fractal and non-fractal features: Nature, v. 341, p.134-138,
228 https://doi.org/10.1038/341134a0

García-Ruiz, J.M., Otálora, F., Sanchez-Navas, A. and Higes-Rolando, F.J., 1994, The formation of manganese dendrites as the mineral record of flow structures, in Renffel, L.O., ED., Fractals and dynamic systems in geoscience: Springer, Berlin, Heidelberg, p. 307-318, DOI: 10.1007/978-3-662-07304-9_23.

Hansel, C.M., 2017, Manganese in marine microbiology. Advances in microbial physiology, v. 70, p. 37-83, DOI: 10.1016/bs.ampbs.2017.01.005.

Haxhimali, T., Karma, A., Gonzales, F. and Rappaz, M., 2006, Orientation selection in dendritic evolution: Nature materials, v. 5, p. 660-664, doi:10.1038/nmat1693.

Hochella Jr, M.F., et al., 2019, Natural, incidental, and engineered nanomaterials and their impacts on the Earth system: Science, v. 363, p. eaau8299, doi:10.1126/science.aau829.

Huang, M., Li, F., Dong, F., Zhang, Y.X. and Zhang, L.L., 2015, MnO2-based nanostructures for high-performance supercapacitors: Journal of Materials Chemistry A, v. 3, p. 21380-21423, DOI: 10.1039/C5TA05523G.

Ivanov, V.K., Fedorov, P.P., Baranchikov, A.Y. and Osiko, V.V.E., 2014, Oriented attachment of particles: 100 years of investigations of non-classical crystal growth: Russian Chemical Reviews, v. 83, p.1204, doi:10.1070/RCR4453.

Krug, J., 1997, Origins of scale invariance in growth processes: Advances in Physics, v. 46, p. 139-282, doi:10.1080/00018739700101498.

Li, D., Yang, J., Tang, W., Wu, X., Wei, L. and Chen, Y., 2014, Controlled synthesis of hierarchical MnO 2 microspheres with hollow interiors for the removal of benzene: RSC Advances, v. 4, p. 26796-26803, doi: 10.1039/C4RA01146E.

McLeish, D.F., Williams-Jones, A.E., Vasyukova, O.V., Clark, J.R. and Board, W.S., 2021, Colloidal transport and flocculation are the cause of the hyperenrichment of gold in nature: Proceedings of the National Academy of Sciences, v. 118, p.e2100689118, https://doi.org/10.1073/pnas.2100689118.

Meakin, P. and Deutch, J.M., 1984, Monte Carlo simulation of diffusion controlled colloid growth rates in two and three dimensions: The Journal of chemical physics, v. 80, p. 2115-2122, doi:10.1063/1.446977.

Meakin, P. and Jamtveit, B., 2010, Geological pattern formation by growth and dissolution in aqueous systems: Proceedings of the Royal Society A: Mathematical, Physical and Engineering Sciences, v. 466, p. 659-694, doi:10.1098/rspa.2009.0189.

Monecke, T., Reynolds, T.J., Taksavasu, T., Tharalson, E.R., Zeeck, L.R., Guzman, M., Gissler, G. and Sherlock, R., 2023, Natural growth of gold dendrites within silica gels: Geology. v. 51, p. 189-192, doi: 10.1130/G48927.1.

Saunders, J. A., Burke, M., & Brueseke, M. E., 2020, Scanning-electron-microscope imaging of gold (electrum) nanoparticles in middle Miocene bonanza epithermal ores from northern Nevada, USA: Mineralium Deposita, v. 55, p. 389-398, https://doi.org/10.1007/s00126-019-00935-y.

Saunders, J.A., 2022, Colloids and nanoparticles: Implications for hydrothermal precious metal ore formation: SEG Discovery, v. 130, p. 15-21. https://doi.org/10.5382/SEGnews.2022-130.fea-01.

Saunders, J.A., and Burke, M., 2017, Formation and aggregation of gold (electrum) nanoparticles in epithermal ores: Minerals, v. 7, p. 163-174, https://doi.org/10.3390/min7090163.

Schoenly, P.A. and Saunders, J.A., 1993, Natural gold dendrites from hydrothermal Au-Ag deposits- Characteristics and computer simulations: Fractals, v. 1, p. 585-593, https://doi.org/10.1142/S0218348X93000617.

Sukop, M.C and Thorne, D.T., 2010, Lattice Boltzmann Modelling: Springer Berlin, Heidelberg.

Szymczak, P. and Ladd, A.J.C., 2006, A network model of channel competition in fracture dissolution: Geophysical Research Letters, v. 33.doi: 10.1029/2005GL025334.

Trivedi, R. and Kurz, W., 1994, Dendritic growth: International Materials Reviews, v. 39, p. 49-74, doi:10.1179/imr.1994.39.2.49.

Tschegg, C., Hou, Z., Rice, A.H.N., Fendrych, J., Matiasek, E., Berger, T. and Grasemann, B., 2020, Fault zone structures and strain localization in clinoptilolite-tuff (Nižný Hrabovec, Slovak Republic): Journal of Structural Geology, v. 138, p. 104090, doi: 10.1016/j.jsg.2020.104090.

Tschegg, C., Rice, A.H.N., Grasemann, B., Matiasek, E., Kobulej, P., Dzivák, M. and Berger, T., 2019, Petrogenesis of a large-scale miocene zeolite tuff in the eastern Slovak Republic: The Nižný Hrabovec open-pit clinoptilolite mine: Economic Geology, v. 114, p. 1177-1194, doi:10.5382/econgeo.4679.

Van Straaten, L.M.J.U., 1978, Dendrites: Journal of the Geological Society, v. 135, p. 137-151, doi:10.1144/gsjgs.135.1.0137.

Voss, R.F., 1984, Multiparticle diffusive fractal aggregation: Physical Review B, v. 30, p.334, doi:10.1103/PhysRevB.30.334.

Welsch, B., Faure, F., Famin, V., Baronnet, A. and Bachèlery, P., 2013, Dendritic crystallization: A single process for all the textures of olivine in basalts?: Journal of Petrology, v. 54, p. 539-574, https://doi.org/10.1093/petrology/egs077.

Yeritsyan, H., et al., 2013. Radiation-modified natural zeolites for cleaning liquid nuclear waste (irradiation against radioactivity): Scientific reports, v. 3, p. 1-7, https://doi.org/10.1038/srep02900.

COMPETING INTERESTS

The authors declare that they have no competing interests.

FIGURE CAPTION

Fig 1. 3D morphology of dendrite forest. (A) Mn dendrites in hand-specimen. (B) µCT image of dendrite forest in clinoptilolite tuff. (C-D) Visualized dendrite trunks (C) and forest base (D) from Fig. 1B. (E) Digital microscope mosaic of polished sample. (F-G) Variations in combined dendrite width (F) and average width (G) with distance from fracture surface.

Fig 2. Structures of individual dendrites. (A) Visualized dendrites showing morphologies from Bi to Biv. (B) Dendrite longitudinal (B1) and horizontal sections (B2). (C-E) SEM-BSE mosaics showing structure of dendrite top (C), middle (D) and base (E). (C'-E') Corresponding porosity maps. (F) Variation of Mn concentration with porosity. (G) Variation of Mn and Si from matrix to core.

Fig 3. Dendrite internal structure. (A-C) SEM-SE images showing structure of Mn oxide particles in dendrites (A-B) and none in matrix (C). (D-E) SEM-BSE images showing details of Mn oxide concentrations from dendrite cores (D), rims (E) to matrix (F). Arrows point to intragranular porosity (D, E). No Mn oxide in matrix (F). Cpt, clinoptilolite.

Fig 4. Dendrite growth models. (A) Numerical (a1-a4) and conceptual (b0-b4) models. Background color gradients in b0-b4 represent particle concentrations; darker colors indicate higher concentrations. (B) Morphological diagram of modeled dendrites. FS, fracture surface.

Figure 1

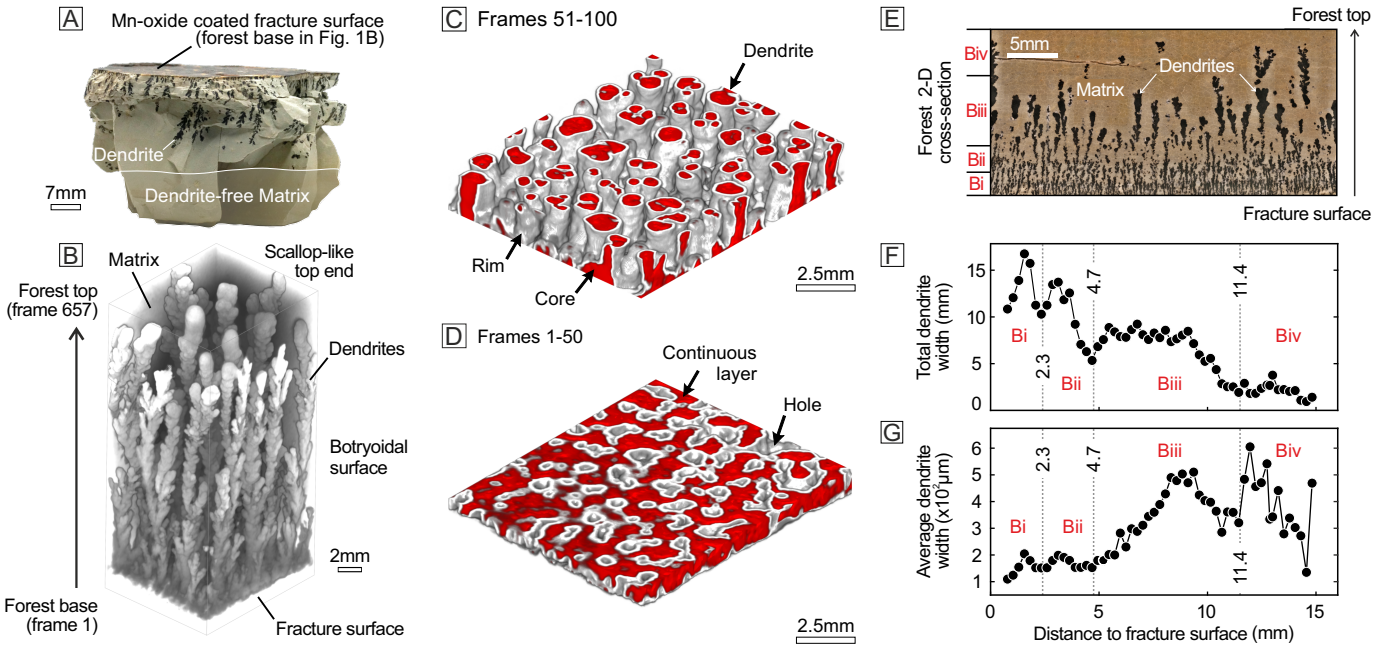
A
Mn-oxide coated fracture surface
(forest base in Fig. 1B)
Dendrite
Dendrite-free Matrix
7mm
B
Matrix
Scallop-like
top end
Forest top
(frame 657)
Dendrites
Botryoidal
surface
2mm
Forest base
(frame 1)
Fracture surface
C
Frames 51-100
Dendrite
Rim
Core
2.5mm
D
Frames 1-50
Continuous
layer
Hole
2.5mm
E
Forest top
5mm
Biv
Biii
Bii
Bi
Dendrites
Matrix
Forest 2-D
cross-section
Fracture surface
F
Total dendrite
width (mm)
15
10
5
0
Bi
Bii
Biii
Biv
2.3
4.7
11.4
G
Average dendrite
width (x10 µm)
6
5
4
3
2
1
0
5
10
15
Distance to fracture surface (mm)

Figure 2

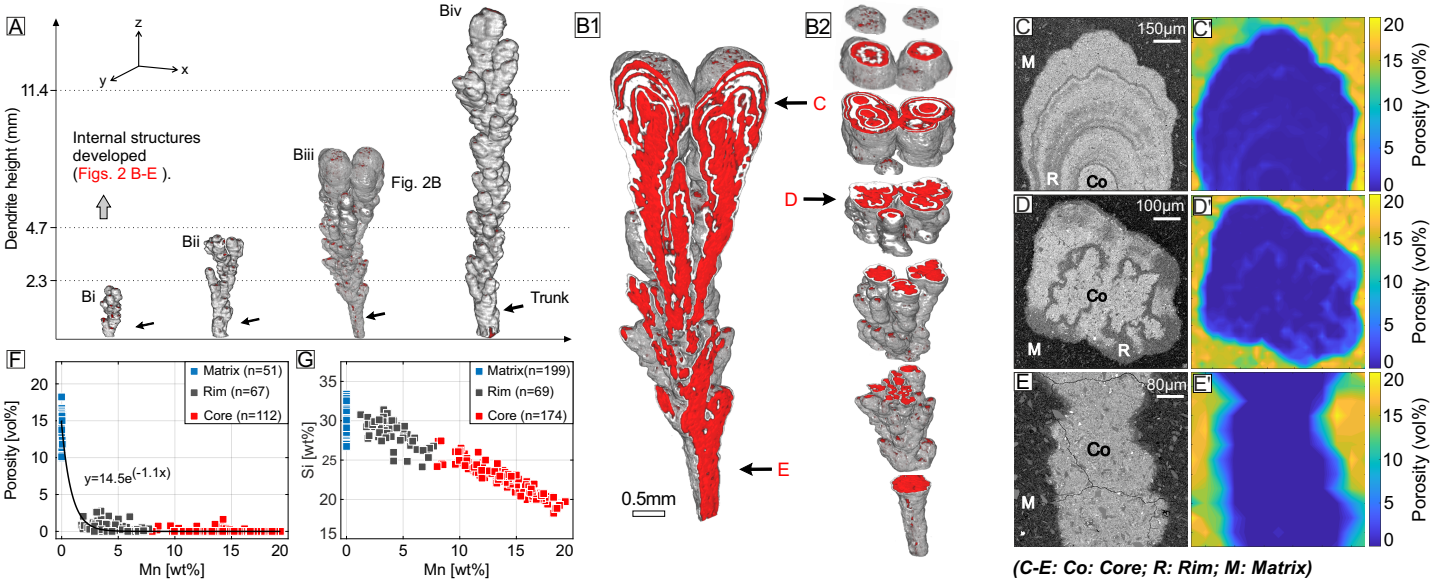

(C-E: Co: Core; R: Rim; M: Matrix)

Figure 3

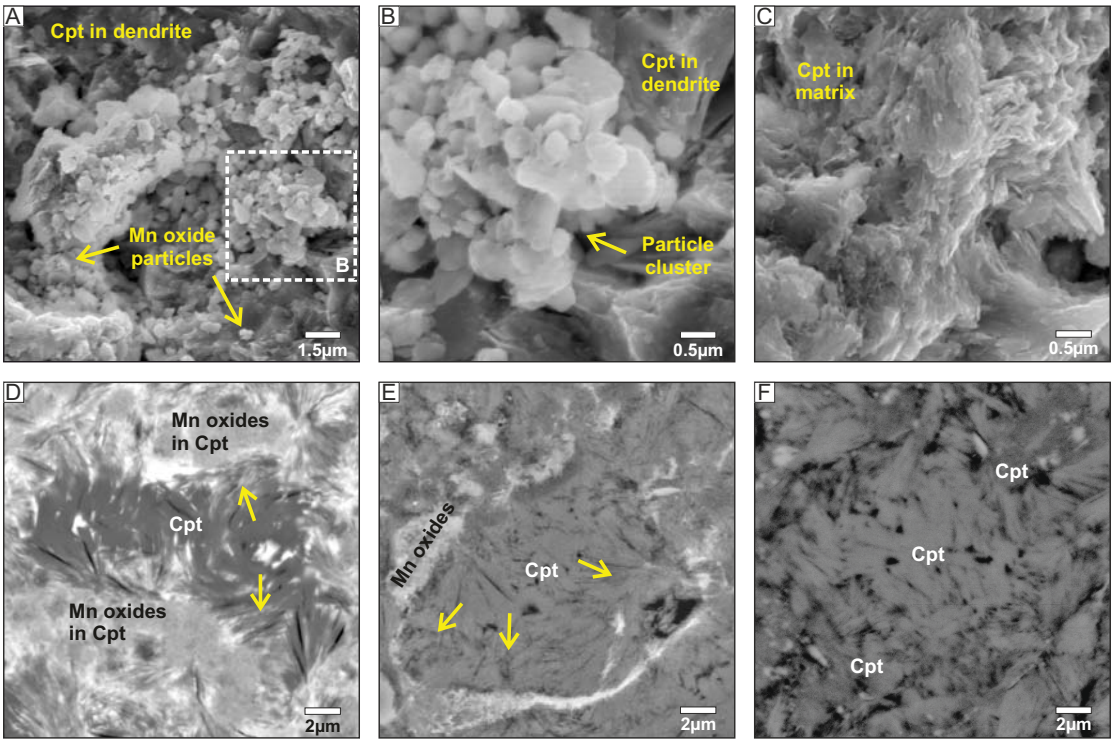
A
Cpt in dendrite
Mn oxide particles
B
1.5µm
B
Cpt in dendrite
Particle cluster
0.5µm
C
Cpt in matrix
0.5µm
D
Mn oxides in Cpt
Cpt
Mn oxides in Cpt
2µm
E
Mn oxides
Cpt
2µm
F
Cpt
Cpt
Cpt
2µm

Fig. 4

Figure 4

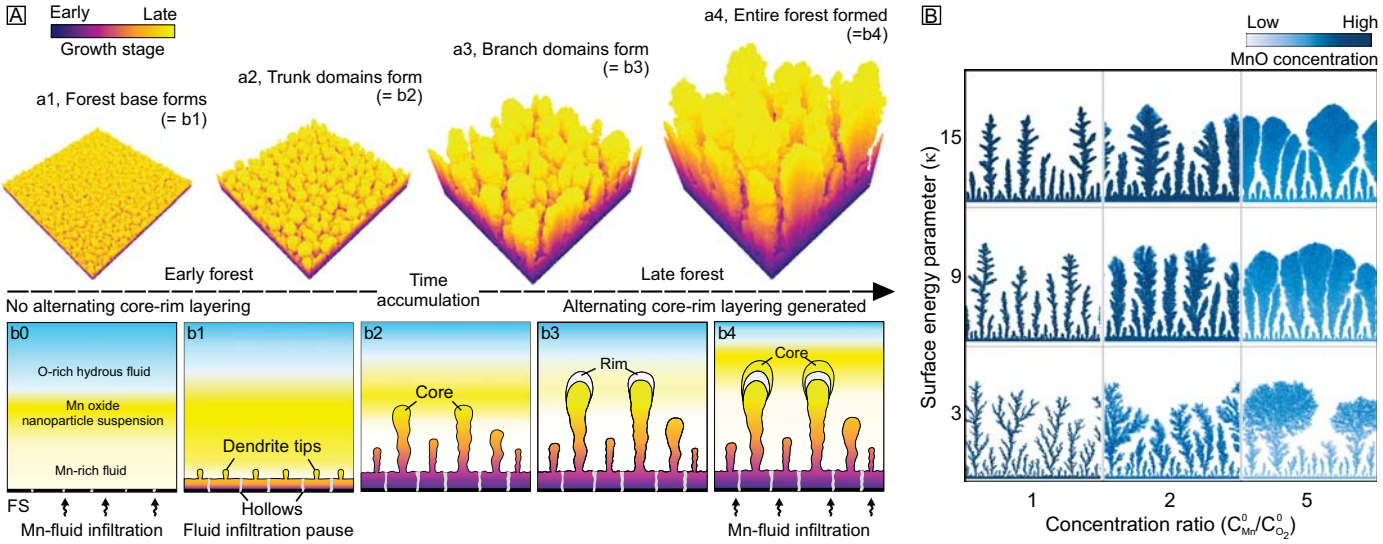

Supplemental Materials for

Three-dimensional mineral dendrites reveal a nonclassical crystallization pathway

Zhaoliang Hou[1], Dawid Woś[2], Cornelius Tschegg[3], Anna Rogowitz[4,1], A. Hugh N. Rice[1], Lutz Nasdala[5], Florian Fusseis[6], Piotr Szymczak[2*], Bernhard Grasemann[1*]

This file includes:

Other supplementary materials for this manuscript include the following:

SUPPLEMENTAL MATERIAL 1. METHODS

32 dendrite samples were collected; seven were scanned using X-ray microtomography, imaging 236 individual mineral dendrites; polished thin-sections of nine specimens were made perpendicular to the fracture surface after being embedded in epoxy resin.

1.1 Structural observations

Three-dimensional microtomographic data were acquired from mm-sized samples at the School of Geosciences, University of Edinburgh. For X-ray imaging, a transmission X-ray source was used with 120 keV peak energy and 2.8 W power loading (W target on diamond). For each dataset, 2000 projections were collected over a 360° sample rotation in evenly spaced intervals, at a 2s exposure for each 1 MP projection. From these projections, virtual image stacks representing the samples were reconstructed with the Octopus v 8.9 software (Dierick et al., 2004), using a filtered back projection algorithm, yielding a stack of 8-bit images (1024×1024 pixels) with a voxel size of 9µm. The image stacks were then processed and visualized using ImageJ (Schneider et al., 2012). The image stacks were denoised using a mean filter (Radius: 1). Dendrite structures were segmented using Weka Trainable Segmentation (Arganda-Carreras et al., 2017). Dendrite forest and internal structures were visualized using 3D script (Schmid et al., 2019). Dendrite volume and 3D fractal dimensions were calculated using "Voxel Counter" and "fractal count" plugins respectively.

Polished thin-sections of dendrites were imaged with a Keyence VHX-5000 digital microscope (DM), using HDR-mode reflected light. The Line-intersection technique was used on binary DM mosaic; successive horizontal straight-lines across each sample at every 100 pixels (~270µm) from the forest bottom to the top, parallel to the fracture surface, were used to calculate total and average dendrite thickness as a function of distance from the fracture surface.

Electron-dispersive X-ray spectroscopy (EDS) and backscattered electron (BSE) imaging were performed on a FEI INSPECT-S50 scanning electron microscope (SEM) with beam conditions of 15 kV and 15 nA. Secondary electron imaging was performed on a FEI QUANTA 3D FEG instrument with beam conditions of 10KV and 4 nA. Binary pore maps were segmented from BSE images using Weka Trainable Segmentation. Porosity variations were calculated by contouring area fractions of the segmented pores (> 90% confidence) from each unit area (307 × 307 pixels).

1.2 Geochemistry

Electron probe micro-analysis (EPMA) line-scan analyses of polished sections were made using a Cameca SXFive FE electron probe micro- analyzer (15 keV acceleration voltage; 20 nA beam current). Detecting beam size was 10 µm in diameter, with an analytical spacing of 10 µm. Detection limit of manganese oxides is 0.05 wt.%.

Raman spectra were obtained using a dispersive Horiba LabRAM HR Evolution system equipped with Olympus BX-series optical microscope and Peltier-cooled, Si-based charge-coupled device detector. The sample material was found to be sensitive to heavy light absorption (i.e. thermal degradation within the focal-spot area, seen from "burned" spots) under 532 nm and 633 nm excitation, and, in addition, spectra obtained with 633 nm excitation were obscured by a fairly intense background. Raman spectra were therefore excited with the 473 nm emission of a diode laser (3 mW at the sample). A 100× objective (numerical aperture 0.90) was used to focus the light onto the sample surface and to collect the Raman-scattered light. The system was operated in the confocal mode, resulting in a lateral resolution of better than 1 µm (cf. Kim et al., 2020). The light to be analyzed was dispersed with a 1800 grooves per mm diffraction grating. More experimental details are described in Zeug et al. (2018).

XRD analyses were done on a Bruker XRD, scanning at 0.015° step intervals and 0.15 s per interval.

1.3 Numerical modelling

Our numerical model is an extension of the classical reaction-diffusion model of 2-D mineral dendrite growth (Chopard, 1991). In detail, we assume that the system was infiltrated by a Mn-rich fluid moving through a fracture network. This fluid invades the rock matrix, pushing an alkaline and oxygenated pore fluid away from the fracture surface. Due to mixing at the interface between the two fluids, a solution oversaturated with manganese oxide appears.

In detail, we are solving the coupled convection-diffusion-reaction equations for the concentrations of oxygen molecules, c_{O_2}, and manganese ions, c_{Mn}. These two species can react with each other, forming nanoparticles of concentration c_p. The equations describing the dynamics of this process are

$$\frac{\partial c_{O_2}}{\partial t} = D_{O_2}\nabla^2 c_{O_2} - k c_{O_2} c_{Mn}$$
$$\frac{\partial c_{Mn}}{\partial t} = D_{Mn}\nabla^2 c_{Mn} - k c_{O_2} c_{Mn}$$

for oxygen molecules and manganese ions and

$$\frac{\partial c_p}{\partial t} = D_p\nabla^2 c_p + k c_{O_2} c_{Mn} - K$$

for the nanoparticles. Similar models have been proposed for the description of Liesegang patterns (Chopard et al, 1994). In the above, D_{O_2}, D_{Mn} and D_p are the diffusion coefficients of oxygen molecules, manganese ions and manganese oxide nanoparticles, respectively. We have assumed that the kinetics of manganese oxide is linear in both concentrations and irreversible with the kinetic reaction rate k. Finally, K is the reaction term taking into account aggregation

of the nanoparticles on the dendrite; the volume fraction of the dendrite, φ_d correspondingly increases as

$$\frac{\partial \varphi_d}{\partial t} = K v_p$$

The reaction term is nonzero only on the dendrite and along its perimeter, and its magnitude depends on the local surface energy of the dendrite, as described in more detail below.

These equations are solved numerically in either square (in 2D) or cubic (in 3D) domains of length *L*, representing the area covered by the pulse of manganese-rich fluid. The initial manganese ion concentration within this region was assumed to be uniform, $c_{Mn}(\mathbf{r}, t=0) = c_{Mn}^0$ and the oxygen concentration was assumed to be zero. On the top boundary of the system, $z = L$, we impose the constant oxygen concentration condition, $c_{O_2}(z = L, t) = c_{O_2}^0$, representing the contact with oxygenated fluid above. The bottom boundary, $z = 0$, is assumed to be impermeable to both Mn and O_2; along other boundaries we impose periodic boundary conditions. The equations are solved using the solute transport lattice-Boltzmann method (Surkop & Thorne, 2006), discretizing the computational domain into the mesh of 250x250 (2D) or 250x250x250 (3D) points. The topology of the mesh in 2D corresponds to two-dimensional nine-speed model (so called D2Q9 - a square lattice with links to both the nearest and diagonal neighbors and with the rest particles), in 3D the corresponding scheme was D3Q27 with the links to 26 nearest and diagonal neighbors in the cubic lattice).

The aggregation of the particles on the dendrite has been implemented in the following way. First, we identify the set of lattice points, $A(t)$, belonging to the aggregate in a given moment of time as well as the perimeter of this set, $\partial A(t)$, i.e. the lattice points neighboring to *A*, which are not taken up by the aggregate yet. We allow the nanoparticles to aggregate both on A and ∂A. In the latter case, however, we require that the concentration of nanoparticles

exceeds a threshold c_p^{th} (nucleation condition). When this condition is fulfilled, the nanoparticles can aggregate in a given point of the perimeter and this point becomes an aggregate point from this time on. Additionally, we set the maximum limit on the manganese oxide volume (per unit volume of the rock) that can be precipitated in a given point, $\varphi_d^{\max} = 0.1$, which is of the order of total porosity of the clinoptilolite matrix. At the beginning of the simulation, the potential nucleation sites of the dendrite correspond to the bottom boundary *(z=0)*, which represents the manganese oxide coated fracture surface, initiating the growth of the mineral dendrite forest.

In the simulations, the ratios of diffusion coefficients of different species were taken to be $D_{Mn} / D_{O_2} = D_p / D_{O_2} = 10$, reflecting the fact that oxygen diffuses faster than the manganese ions and nanoparticles.

In the numerical model, the aggregation itself proceeds in a probabilistic manner, with the local concentration of nanoparticles transferred to a dendrite with a probability that depends on the local radius curvature of the dendrite, R (Vicsek, 1984),

$$p = p_0 + \frac{\Gamma}{R}$$

where $\Gamma = \frac{\sigma v_m}{kT}$ is the capillarity constant, in which σ is the interfacial free energy, v_m is the precipitate molecular volume, k is the Boltzmann constant, and T is the absolute temperature (Mullins and Sekerka, 1963). The local radius of curvature, R, is estimated based on the number of lattice sites occupied by the dendrite in the neighborhood of a given point (Vicsek, 1984; Kadanoff, 1985, Liang, 1985) and $p_0 = \frac{1}{2}$.

There are two important length scales in diffusion-controlled growth processes, the diffusive length, $\lambda_d = \frac{D_p}{U}$, which is the ratio of the average growth velocity and diffusion constant and chemical capillary length $\lambda_c = \gamma\Gamma$, where γ is the acid capacity number defined as the number of manganese oxide molecules per unit volume of a dendrite to the number of manganese oxide molecules per unit volume of the precipitating solution (Mullins and Sekerka, 1963, Meakin, 1998, Ladd & Szymczak 2021). The length scales characterizing the morphology of the dendritic forest, λ_m, such as the width of the dendrites or separation between them, are, to the first approximation given by the geometric mean between λ_c and λ_d (Meakin, 1998)

$$\lambda_m = \sqrt{\lambda_c \lambda_d} = \sqrt{\kappa}\lambda_d$$

where $\kappa = \lambda_c / \lambda_d$ is the ratio of the capillary and diffusive length.

The other important parameter in our system is the ratio of the initial Mn concentration to the oxygen concentration imposed on the top boundary of the system, $c^0_{Mn}/c^0_{O_2}$, and the ratio of nucleation concentration of manganese oxide particles to the oxygen concentration, $c^{th}_p/c^0_{O_2}$ (Fig. S1A). Since we

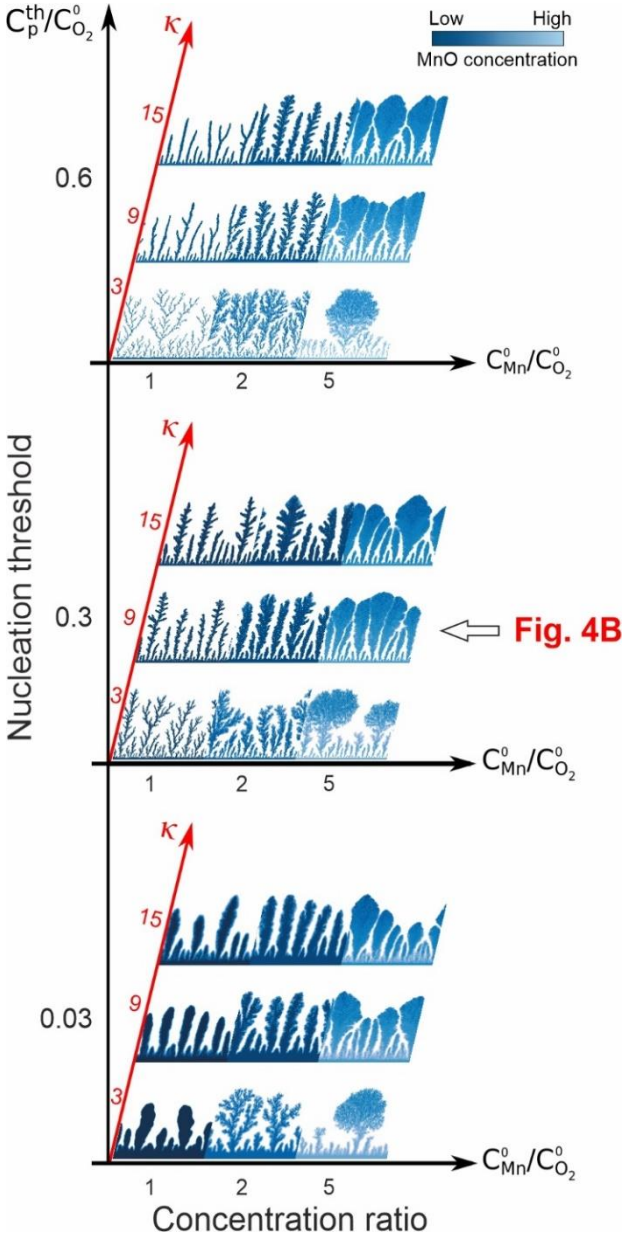

Fig. S1A

Morphologies 2D dendritic patterns as a function of Mn and O_2 concentration ratio and, capillary and diffusive length ratio and the nucleation threshold concentration.

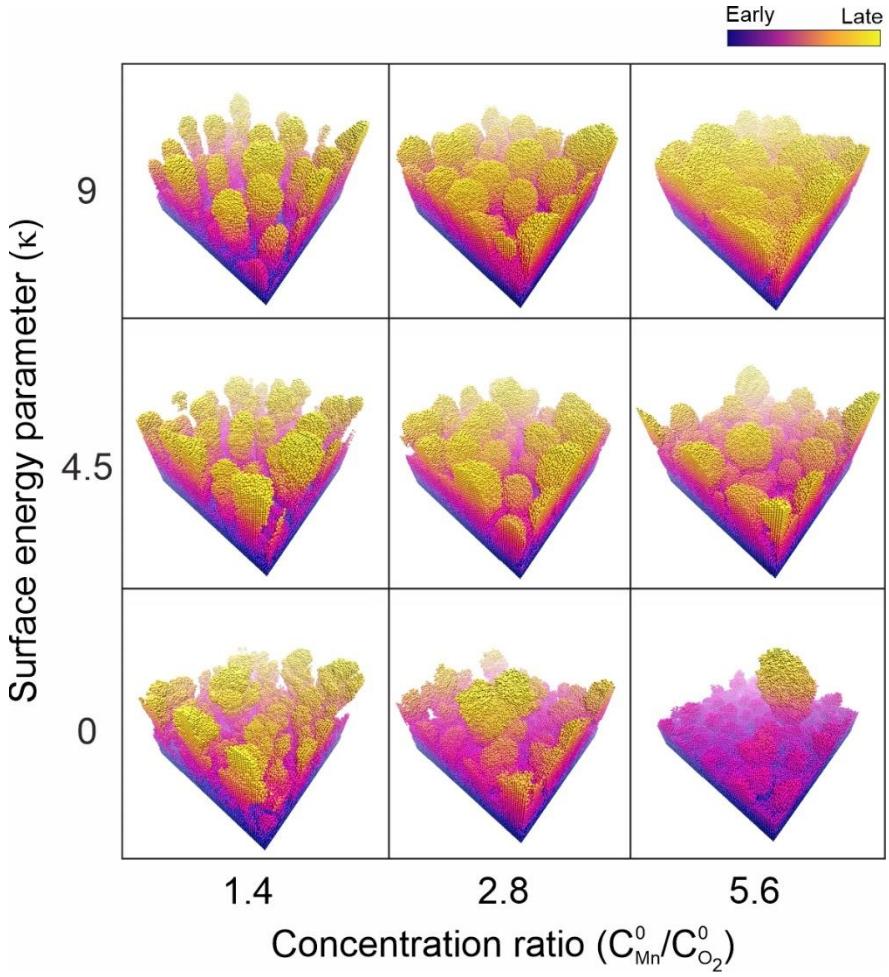

Fig. S1B. Morphologies 3D dendritic patterns. Simulation based on the parameters defined by the 2D simulations.

do not have information what the values of these parameters were in the real system, we analyzed the morphologies of the dendrites for a range of different values of these three ratios ($\kappa, c^0_{Mn}/c^0_{O_2}, c^{th}_p/c^0_{O_2}$) as presented in Supplemental material Fig S4. The comparison of the resulting morphologies with that of the natural dendrite forest in clinoptilolite led us to the conclusion that the latter is characterized by $\kappa \approx 9, c^0_{Mn}/c^0_{O_2} \approx 1-2, c^{th}_p/c^0_{O_2} \approx 0.3$. These estimates will be further modified by the dimensionality of the system. In particular, in 3D the capillary effects (for the same Γ) are two times stronger in 3D than in 2D, hence we expect that κ should be two times smaller in the 3D case, as indeed confirmed in 3D simulations (see Fig. S1B), which show that the morphologies similar to the natural ones are obtained for $\kappa \approx 4.5$, $c^0_{Mn}/c^0_{O_2} \approx 1-2, c^{th}_p/c^0_{O_2} \approx 0.3$

SUPPLEMENTAL MATERIAL FIG. S2. SAMPLE DESCRIPTION

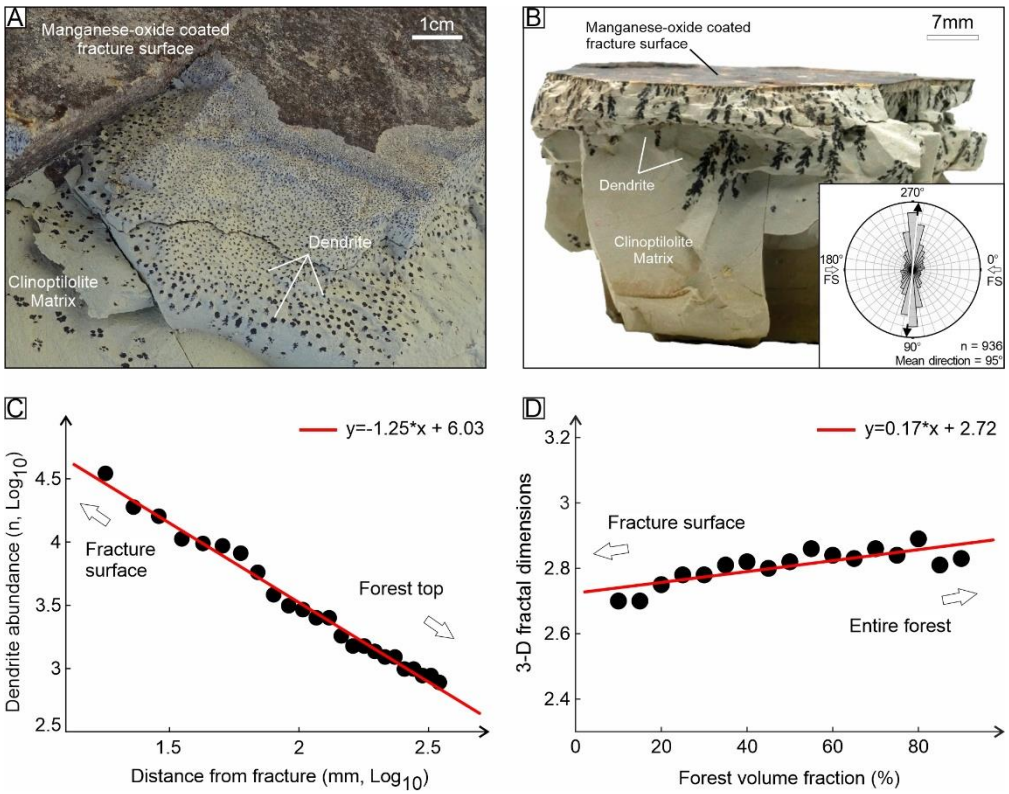

Overview of mineral dendrites in clinoptilolite-tuff. **A**, Irregular surface cutting in-situ clinoptilolite, showing horizontal, oblique and longitudinal sections through the dendrites, revealing their 3-D geometry. **B**, Hand-specimen (also shown in Fig. 1A) showing localization of the mineral dendrites adjacent to a manganese oxide-coated fracture surface, and their branching architecture. Rose-diagram showing dendrite preferred growth orientation relative to the fracture surface (FS). Black arrows with the white line indicate the 095°-275° mean orientation of dendrites, approximately perpendicular to the fracture surface (0°-180°, white arrows). **C**, Power-law scaling of variation in dendrite abundance (n) as forest height increases. Note α is ~1.25. **D**, Variation of forest 3-D fractal dimension as the forest volume increases from the fracture surface. Calculations for both C and D are based on µCT data.

SUPPLEMENTAL MATERIAL FIG. S3. DENDRITE GEOCHEMISTRY DATA

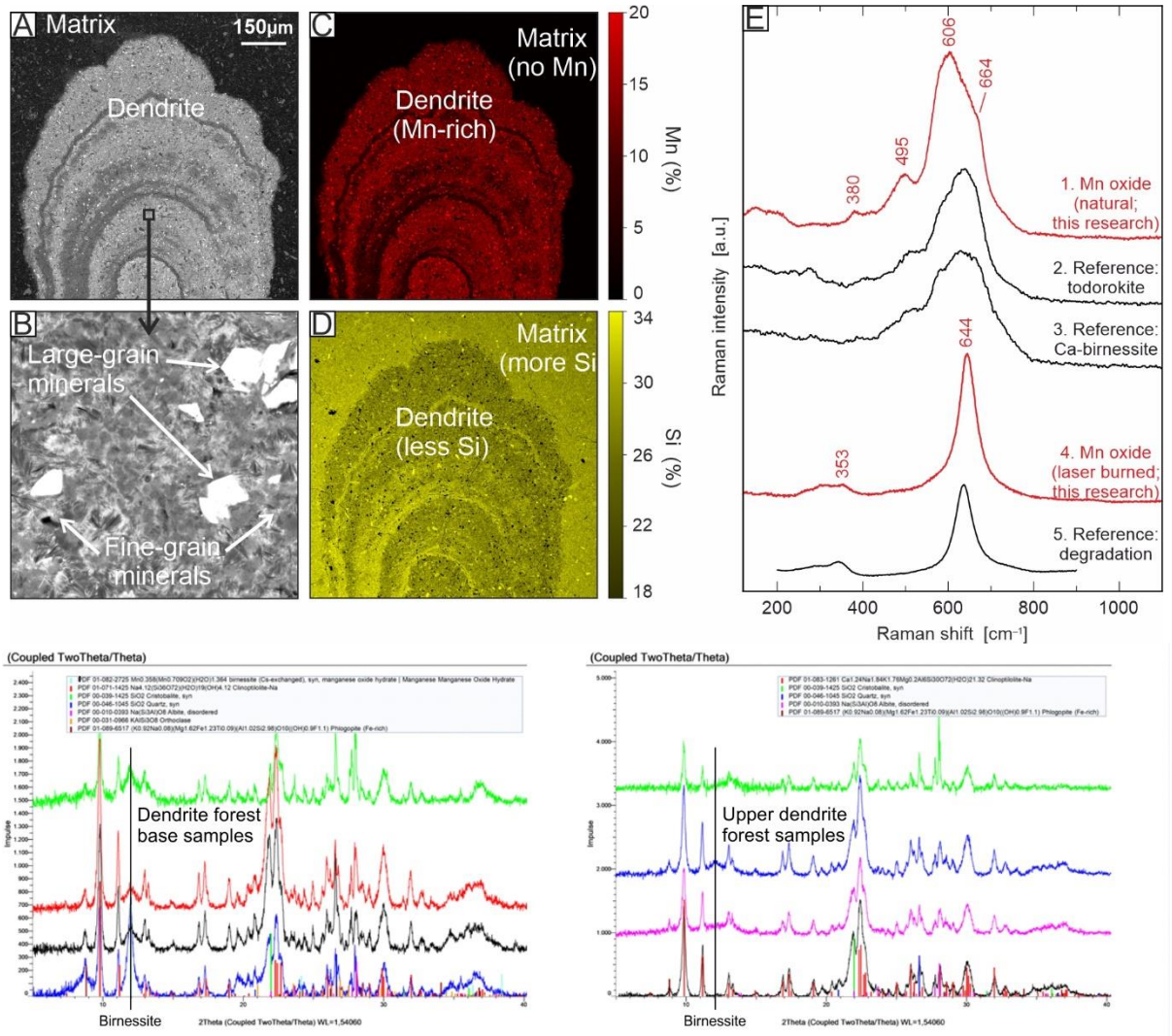

Overview of dendrite-forming manganese oxides. A, SEM-BSE showing the top part of a mineral dendrites. For details of dendrite internal structure (banding) see the main text and Fig. 2. B, Enlargement of A. Dendrites comprise fine-grained minerals with euhedral larger minerals. The larger minerals were analysed by Raman spectroscopy. C-D, SEM-EDS maps showing dendrite-forming materials; both the fine- and larger-grained minerals are dominated by manganese. E, Raman spectra of larger minerals. Top three spectra are low-energy 473 nm excitation; bottom two, high-energy 532 nm excitation. 1 and 4 show the natural Mn oxide from the dendrites. 2 and 3 are reference spectra of poorly ordered todorokite and Ca-birnessite

(Abrashev et al., 2019). Reference spectrum of laser-pyrolysed MnO_2 (degradation) from Bernardini et al., 2019.

Reliable assignment to a certain mineral species is virtually impossible, since: (i) spectra depend appreciably on the degree of crystallinity; (ii) spectra of different Mn-oxide minerals show broad similarities, and virtually contradictory spectra are found for the same mineral in the literature; (iii) natural Mn oxides often are heterogeneous mixtures of several phases; and (iv) Mn minerals are sensitive to local heating due to absorption of laser light. In spite of these uncertainties, our spectrum may be assigned to a hydrated Mn-dominated oxide, such as birnessite or todorokite (Julien et al., 2004; Abrashev et al., 2019). see also the spectra of a low-grade Mn ore of Pani et al. (2015). This assignment is apparently supported by the observation that our sample, after thermal degradation due to intense green-laser illumination, yielded a spectrum that is broadly similar to that of green-laser-decomposed pyrolusite (β–MnO2; see Bernardini et al., 2019).

X-ray diffraction of powdered samples derived by drilling 4 samples, each with a dendrite forest base powder and a upper dendrite forest powder. Low peak intensities indicate that most of the manganese is amorphous. Minor peak intensities reveal birnessite as a typical component in the dendrite forest base and a minor component in one samples from the upper dendrite forest.

Thus both Raman spectroscopy and XRD analyses indicate that there is at least some Mn oxyhdroxides in the dendrites. Whether the amorphous material is an oxyhdroxide is unknown.

SUPPLEMENTAL MATERIAL FIG. S4. NUMERICAL Vs. NATURAL DENDRITES

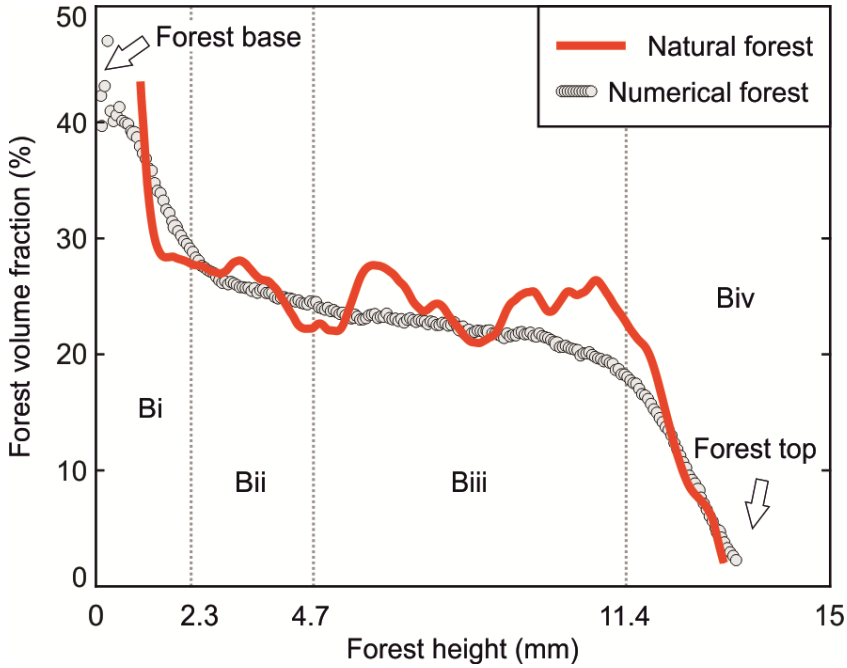

Comparison of volume fractions in the natural and numerical dendrite forest. Numerical dendrite forest shows a similar volume fraction and volume fraction changes to the natural sample. Forest height is the distance from the fracture surface.

REFERENCE FOR SUPPLEMENTARY MATERIALS

Abrashev, M.V., Chernev, P., Kubella, P., Mohammadi, M.R., Pasquini, C., Dau, H. and Zaharieva, I., 2019, Origin of the heat-induced improvement of catalytic activity and stability of MnO x electrocatalysts for water oxidation: Journal of Materials Chemistry A, v. 7, p.17022-17036, doi:10.1039/C9TA05108B.

Arganda-Carreras, I., Kaynig, V., Rueden, C., Eliceiri, K.W., Schindelin, J., Cardona, A. and Sebastian Seung, H., 2017, Trainable Weka Segmentation: a machine learning tool for microscopy pixel classification: Bioinformatics, v. 33, p. 2424-2426, doi:10.1093/bioinformatics/btx180.

Bernardini, S., Bellatreccia, F., Municchia, A.C., Della Ventura, G., Sodo, A., 2019, Raman spectra of natural manganese oxides: Journal of Raman Spectroscopy, v. 50, p. 873–888, doi:10.1002/jrs.5583.

Chopard, B., Herrmann, H.J. and Vicsek, T., 1991, Structure and growth mechanism of mineral dendrites: Nature, v. 353, p. 409-412, DOI:10.1038/353409a0.

Chopard, B., Luthi, P., & Droz, M., 1994, Microscopic approach to the formation of Liesegang patterns: Journal of statistical physics, v. 76, p. 661-677, doi:10.1007/BF02188680.

Dierick, M., Masschaele, B. and Van Hoorebeke, L., 2004, Octopus, a fast and user-friendly tomographic reconstruction package developed in LabView®: Measurement Science and Technology, v. 15), p. 1366, doi:10.1088/0957-0233/15/7/020.

Julien, C.M., Massot, M. and Poinsignon, C., 2004, Lattice vibrations of manganese oxides: Part I. Periodic structures. Spectrochimica Acta Part A: Molecular and Biomolecular Spectroscopy, v. 60), p. 689-700, 10.1016/S1386-1425(03)00279-8.

Kadanoff, L. P., 1985, Simulating hydrodynamics: a pedestrian model: Journal of statistical physics, v. 39, p. 267-283, doi:10.1007/BF01018663.

Kim, Y., Lee, E.J., Roy, S., Sharbirin, A.S., Ranz, L.-G., Dieing, T., Kim, J., 2020, Measurement of lateral and axial resolution of confocal Raman microscope using dispersed carbon nanotubes and suspended graphene: Current Applied Physics, v. 20, p. 71–77, doi:10.1016/j.cap.2019.10.012.

Ladd, A. J., & Szymczak, P., 2021, Reactive flows in porous media: Challenges in theoretical and numerical methods: Annual Review of Chemical and Biomolecular Engineering, v. 12, p, 543-571, doi: 10.1146/annurev-chembioeng-092920-102703.

Liang, S., 1986, Random-walk simulations of flow in Hele Shaw cells: Physical Review A, v. 33, p. 2663, doi:10.1103/PhysRevA.33.2663.

Meakin, P., 1998, Fractals, scaling and growth far from equilibrium, Volume 5: Cambridge, Cambridge university press, 674p.

Mullins, W. W., and Sekerka, R. F., 1963, Morphological stability of a particle growing by diffusion or heat flow: Journal of applied physics, v. 34, p. 323-329, doi:org/10.1063/1.1702607.

Pani, S., Singh, S.K., Mohapatra, B.K., 2015, Vibrational spectroscopic study for qualitative assessment of Mn-oxide ore: Resource Geology, v. 66, p. 12–23, doi:10.1111/rge.12083.

Schmid, B., Tripal, P., Fraaß, T., Kersten, C., Ruder, B., Grüneboom, A., Huisken, J. and Palmisano, R., 2019, 3Dscript: animating 3D/4D microscopy data using a natural-language-based syntax: Nature methods, v. 16, p. 278-280, doi:10.1038/s41592-019-0359-1.

Schneider, C.A., Rasband, W.S. and Eliceiri, K.W., 2012, NIH Image to ImageJ: 25 years of image analysis: Nature methods, v. 9, p. 671-675, doi:10.1038/nmeth.2089.

Sukop, M.C and Thorne, D.T., 2010, Lattice Boltzmann Modelling: Springer Berlin, Heidelberg.

Vicsek, T., 1984, Pattern formation in diffusion-limited aggregation: Physical review letters, v. 53, p. 2281, doi :10.1103/PhysRevLett.53.2281.

Zeug, M., Nasdala, L., Wanthanachaisaeng, B., Balmer, W.A., Corfu, F. and Wildner, M., 2018, Blue zircon from Ratanakiri, Cambodia: Journal of Gemmology, v. 36, p. 112–132, doi:10.15506/JoG.2018.36.2.112.